

Influence of solvent molecular geometry on the growth of nanostructures

Ammara Ejaz^{a,b}, Jong H. Han^{b,*}, Ravinder Dahiya^a

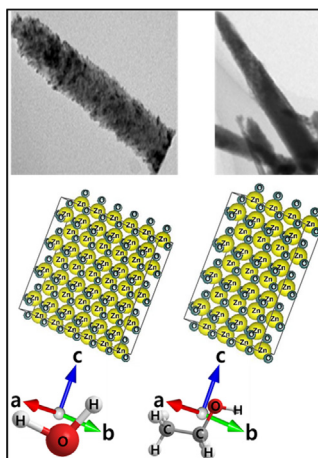
^a Bendable Electronics and Sensing Technologies (BEST) Group, James Watt School of Engineering, University of Glasgow, G12 8QQ, UK

^b Nanocarbon Convergence Materials Lab (NCML), School of Chemical Engineering, Chonnam National University, Gwangju 500-757, Republic of Korea

HIGHLIGHTS

- Influence of water and ethanol molecular geometry on the growth mechanism of ZnO nanorods.
- Role of carbon chain length as a limiting factor for ZnO monomer stacking in wurtzite crystal system.
- New theory Formulation based on solvent molecular geometry to predict the aspect ratio of nanorods.
- Nitrogen doping Influence on the synthesis and stabilization of ZnO monomer for nanorods formation.

GRAPHICAL ABSTRACT



ARTICLE INFO

Article history:

Received 29 January 2020

Revised 27 February 2020

Accepted 28 February 2020

Available online 3 March 2020

Keywords:

Graphene oxide
Molecular geometry
Solvent
ZnO nanorods
Growth Kinetics

ABSTRACT

Solvent properties such as surface tension, dielectric constant, and viscosity have been extensively studied over more than 150 years to understand their influence on the growth kinetics of nanostructures. Interestingly, these nanoparticles-based studies have missed the influence of solvent molecular geometry. Herein, by synthesizing ZnO nanorods on a highly conductive nitrogen incorporated graphene oxide (N-GO) substrate, we present the first study showing the influence of solvent molecular geometry on the growth mechanism of nanostructures. The solvents such as water (N-GO-ZnO-W) allow a large number of functional atoms along a, b and c-axis to coordinate in all possible directions with the metal ions of wurtzite hexagonal crystal system of ZnO and thus leads to lower aspect ratio nanorods. On the contrary, the unavailability of binding sites along a-axis for solvents such as ethanol (N-GO-ZnO-E) provides a size-limiting effect and leads to preferred growth along b and c-axis, thus generating ZnO nanorods with a higher aspect ratio. The study shows that the number of interacting atoms, carbon chain length and the solvent molecular geometry influence the aspect ratio and therefore a solvent could be used to tune the nanostructures morphology and hence the performance of devices based on them.

© 2020 The Author(s). Published by Elsevier Inc. This is an open access article under the CC BY license (<http://creativecommons.org/licenses/by/4.0/>).

* Corresponding author.

E-mail addresses: jghan@chonnam.ac.kr (J.H. Han), Ravinder.Dahiya@glasgow.ac.uk (R. Dahiya).

1. Introduction

Nanostructures with various materials and morphologies such as nanowires [1], nanorods [2], nanobelts [3], nanosheet [4], nanocable [5], and nanocomb [6], etc. have attracted significant attention for application in electrochemical sensing, biosensing and energy storage etc [7–12]. Morphologies such as nanorods offer higher aspect ratios (length to width ratio) and hence the large surface-to-volume ratio, which is needed for enhanced performance of devices made from them. To this end, a wide variety of physical (chemical vapor deposition, molecular beam epitaxy, pulsed laser deposition, magnetron sputtering, and thermal evaporation) and chemical (chemical bath deposition, electrochemical deposition, hydrothermal, solvothermal, sol-gel, and precipitation) methods have been explored [13–18]. These methods involve controlling the process parameters such as temperature, deposition time, stirring speed, reducing agent, vacuum condition, catalysts, concentration and solvent, etc. to obtain nanostructures with desired aspect ratio. Additionally, the influence of ambient conditions such as solvent properties such as surface tension, dielectric constant, pH, and viscosity etc. has been studied for the growth mechanism of nanostructures [18,19]. Interestingly, none of these extensive nanoparticles (NPs)-based studies conducted over more than 150 years has considered the influence of solvent molecular geometry on the growth of nanostructures and their morphology. Herein, with ethanol and water solvents we demonstrate for the first time the influence of solvent molecular geometry on the aspect ratio of nanostructures such as ZnO nanorods. The ethanol (N-GO-ZnO-E) and water (N-GO-ZnO-W) are selected here due to the availability of different number of interacting atoms and molecular geometries. The ZnO used here presents an ideal testbed to gain insight into nanoparticles growth mechanism, as it carries

3d transition metal ions and offers a rich family of structures such as whiskers, wires, rods, tubes, belts, cages, rings, combs, prisms, etc. [20–25]. The ZnO nanorods were synthesized on a highly conductive nitrogen incorporated graphene oxide (N-GO) substrate (shown in Fig. 1), in water and ethanol solvents. The synthesis steps include the dual interaction of 1,4-Phenylenedimethanamine carrying two NH_2 groups on the opposite position of a benzyl ring. NH_2 groups are expected to covalently react with the hydroxyl, epoxy, and carboxyl groups of GO in a series of reduction and condensation reactions to produce pyridinic, pyrrolic, graphitic-N and pyridinic-NO species [26–28]. These nitrogen configurations have already been shown to alter the GO chemistry by the redistribution of electronic charges in the π electronic system of GO matrix [29,30]. Nitrogen doping intrinsically modifies the material chemistry by the generation of electrophilic and nucleophilic centers in the vicinity of heteroatom [27], which, consequently, plays a vital role in the concentration and growth kinetics of NPs [31]. The synthesized NPs were extensively studied through X-ray photoelectron spectroscopy (XPS), high resolution transmission electron microscopy (HR-TEM), X-ray diffraction (XRD), energy dispersive X-ray spectroscopy (EDX) and EDX mapping.

2. Experimental

2.1. Chemicals and reagents

Graphite powder (~325 mesh, 99.999%), 1,4-Phenylenedimethanamine, ZnCl_2 , $\text{N}_2\text{H}_4 \cdot \text{H}_2\text{O}$ (64 – 65%), and $\text{C}_2\text{H}_5\text{OH}$ (99.99%), were purchased from Sigma-Aldrich Chemical Co., South Korea. KMnO_4 , H_3PO_4 , and H_2SO_4 were purchased from Daejung Co., South Korea. Deionized water was used from Elix

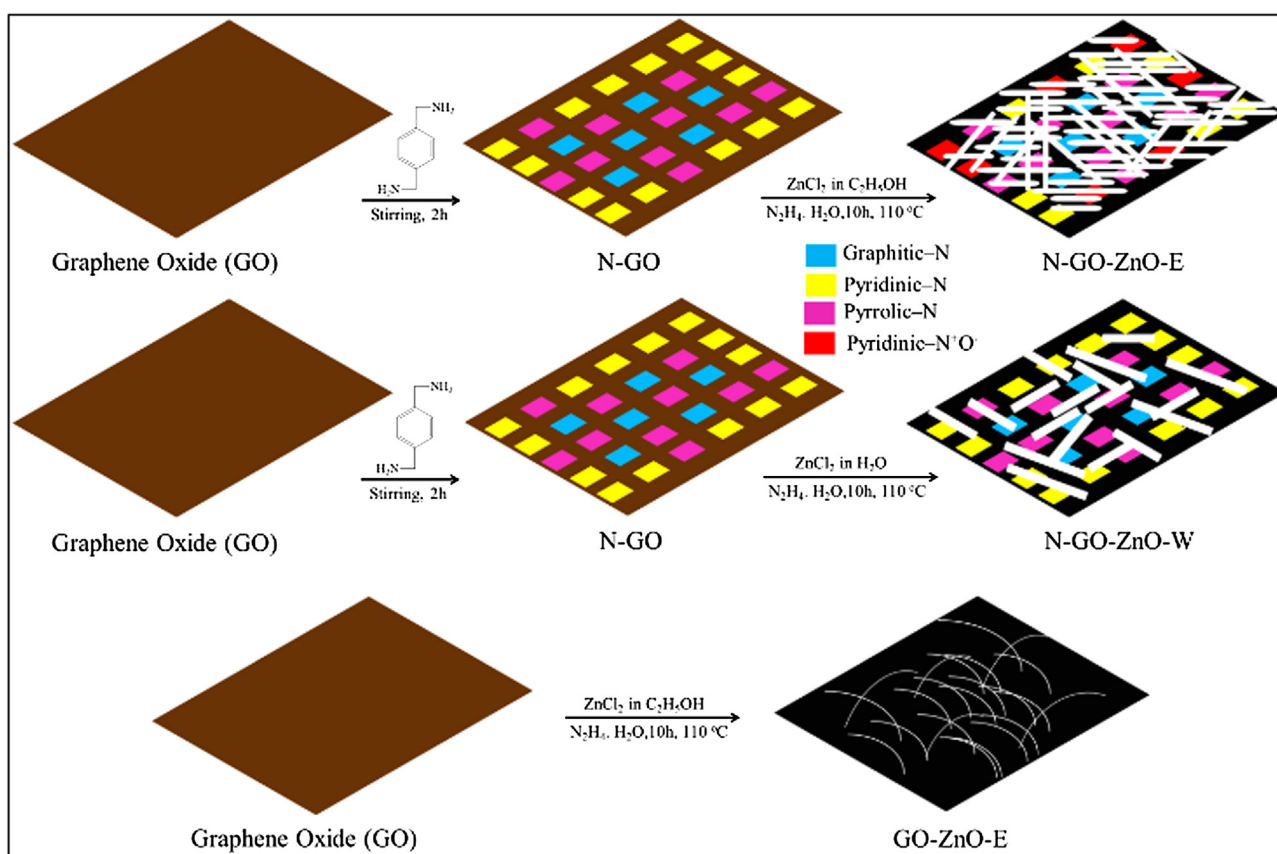


Fig. 1. The schematic illustration of N-GO-ZnO-E and N-GO-ZnO-W, and GO-ZnO-E synthesis.

Reference Water Purification System. All the reagents used in this experiment were of analytical grade and were used without further purification.

2.2. Instrumentation

The structural characterization of the nanomaterials were carried out using X-ray photoelectron spectroscopy (XPS) on a Multi-Lab 2000 spectrometer (Thermo VG Scientific, Southend-On-Sea, Essex, UK) in an ultra-high vacuum chamber along with X-ray diffraction (XRD) spectrum carried out on a Rigaku D/max-2500, using filtered Cu K α radiation at Center for Research Facilities (CCRF) of Chonnam National University (CNU). The high-resolution transmission electron microscopy (HR-TEM) and energy dispersive X-ray spectroscopy (EDX) were studied using a JEM-2100F microscope at 200 kV in the Korea Basic Science Institute (KBSI) of CNU.

2.3. Synthesis of nanomaterials

GO was synthesized from natural graphite powder (~325 mesh, 99.999%) according to the improved Hummer's method [38]. The synthesis of *N*-GO-ZnO-E, *N*-GO-ZnO-W, and GO-ZnO-E nanomaterial is shown in Fig. 1. Initially, GO was dispersed in double distilled water (1 mgmL⁻¹) and sonicated for 1 h. The resulting homogeneous suspension was mixed with an aqueous solution of 1,4-Phenylenedimethanamine (1 mgmL⁻¹) in a round-bottom flask equipped with a magnetic stirrer bar. After 2 h of continuous stirring, a solution of ZnCl₂ in ethanol was added to the homogeneous solution and kept for 30-minute stirring. Thereafter, 100 μ L of N₂H₄·H₂O was added as a reducing agent followed by stirring and heating at 110 °C for the next 10 h. The black solution obtained was filtered three times with double distilled water and was dried under vacuum at 50 °C for overnight. The *N*-GO-ZnO-W was prepared in the same protocol, except ZnCl₂ solution was prepared in water rather than in ethanol. GO-ZnO-E was also prepared in the same protocol except with the addition of 1,4-Phenylenedimethanamine.

3. Results and discussion

3.1. Structural analysis of *N*-GO-ZnO-W and *N*-GO-ZnO-E

The crystallinity of the *N*-GO-ZnO-W and *N*-GO-ZnO-E were evaluated from the XRD spectra. As can be seen in Fig. 2, both

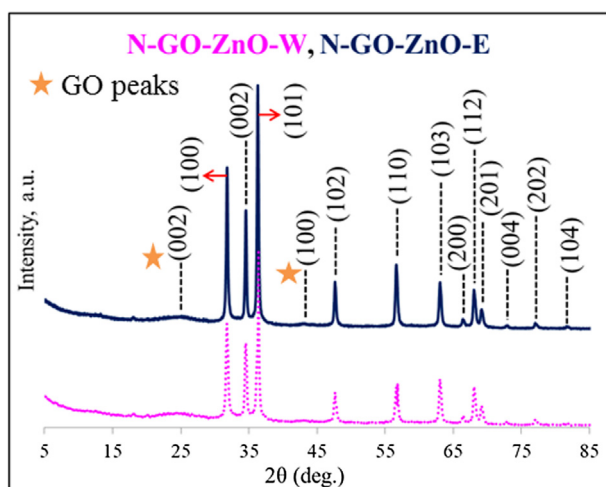


Fig. 2. XRD spectra of the *N*-GO-ZnO-W and *N*-GO-ZnO-E nanomaterials.

nanomaterials showed several broad peaks signifying the small size of the ZnO NPs. The pronounced diffraction reflections at 31.78°, 34.54°, 36.28°, 47.61°, 56.59°, 63.01°, 66.36°, 68.01°, 68.19°, 72.99°, 77.01°, and 81.58° having inter-atomic spacing (*d*) of 0.28, 0.26, 0.24, 0.19, 0.16, 0.15, 0.14, 0.13, 0.13, 0.12, 0.12 and 0.17 nm respectively, showed an agreement with Wurtzite hexagonal crystal structure of ZnO [8,32]. The enhanced diffraction peaks of (1 0 0), (0 0 2), (1 0 1) and (1 0 3) crystal faces indicate a polycrystalline behavior, accommodated with preferential ZnO crystal orientation along the *c*-axis which provides hexagonal rod-like morphology. The high diffraction intensity of (0 0 2) in *N*-GO-ZnO-E represents growth of ZnO nanorods with a high aspect ratio which was also observed from HRTEM study. Further, the absence of any impure peak suggested the synthesis of pure hexagonal structured ZnO in both nanomaterials. Besides, a GO reduction reflection at 26.1° and honeycomb structure formation by the sp² hybridized carbon reflection at 42.9° with a '*d*' spacing of 0.34 and 0.21 nm respectively [33] confirmed the XPS results regarding the successful integration of 1,4 Phenylenedimethanamine into GO network.

In order to better understand the obtained oxidation states and peak intensities of *N*-GO-ZnO-W and *N*-GO-ZnO-E nanomaterials by XPS, it is important to understand the expected chemical reactions between 1,4-Phenylenedimethanamine and GO. Following nitrogen configurations are expected to obtain from the reaction between GO oxygenated functionalities and NH₂ group of 1,4-Phenylenedimethanamine.

- (i) Reduction of epoxy and OH group of GO by NH₂ to produce graphitic-N and pyrrolic-N respectively.
- (ii) A reaction between the -COOH and NH₂ to produce pyridinic-N.

Fig. 3a shows the XPS survey spectra of *N*-GO-ZnO-W and *N*-GO-ZnO-E, which is clearly revealing the presence of nitrogen (N1s), and zinc (Zn2p_{1/2}, Zn2p_{3/2}) along with the expected carbon (C1s) and oxygen (O1s) atoms from the corresponding peaks at 400.1, 1045.37, 1022.3, 285.16 and 532.04 eV (*N*-GO-ZnO-E), and 399.47, 1044.9, 1021.9, 284.43 and 531.35 eV (*N*-GO-ZnO-W) respectively [34,35]. Zn and O1s peaks of *N*-GO-ZnO-E exhibited comparatively stronger intensity than *N*-GO-ZnO-W, thus; suggesting the presence of a higher proportion of Zn and O atom in its electronic environment. The survey spectra of both nanomaterials were deconvoluted to figure out the mechanism of ZnO nanorods morphology and growth kinetics by understanding the individual oxidation state of each atom present in the system. C1s spectra in Fig. 3b (*N*-GO-ZnO-E) and b' (*N*-GO-ZnO-W) showed corresponding peaks of sp³-C, sp²-C, C-O and O-C=O at 284.78, 285.7, 287.64, 290.07 eV, and at 284.79, 285.67, 287.82, 290.67 eV respectively [31]. The N1s spectra in Fig. 3c (*N*-GO-ZnO-E) and c' (*N*-GO-ZnO-W) exhibited distinctive peaks at 399.07, 400.04, 401.13 eV, and 399.29, 400.43, 402.08 eV revealing the presence of pyridinic-N, pyrrolic-N, and graphitic-N respectively [36]. However, N1s spectrum of *N*-GO-ZnO-E showed an additional peak at 402.38 eV which indicates the presence of pyridinic-N⁺O⁻ [37] (The reason behind the emergence of this additional pyridinic-N⁺O⁻ peak will be explained later in the ZnO nanorods formation discussion). The higher intensity of pyridinic-N (Fig. 3c') justifies the low intensity of O-C=O peak (Fig. 3b'), and vice versa for the additional peak of O-C=O (Fig. 3b) at 292.52 eV. Fig. 3d (*N*-GO-ZnO-E) and d' (*N*-GO-ZnO-W) show O1s spectra with the appearance of C-O, -OH, and H₂O at 531.31, 532.35, 533.38 eV, and 531.34, 532.28, and 533.27 eV respectively [38,39]. The higher intensity of graphitic-N and lower intensity of pyrrolic-N (Fig. 3c) is justifying the low intensity of C-O and high intensity of OH (Fig. 3d), and vice versa for the lower graphitic and higher

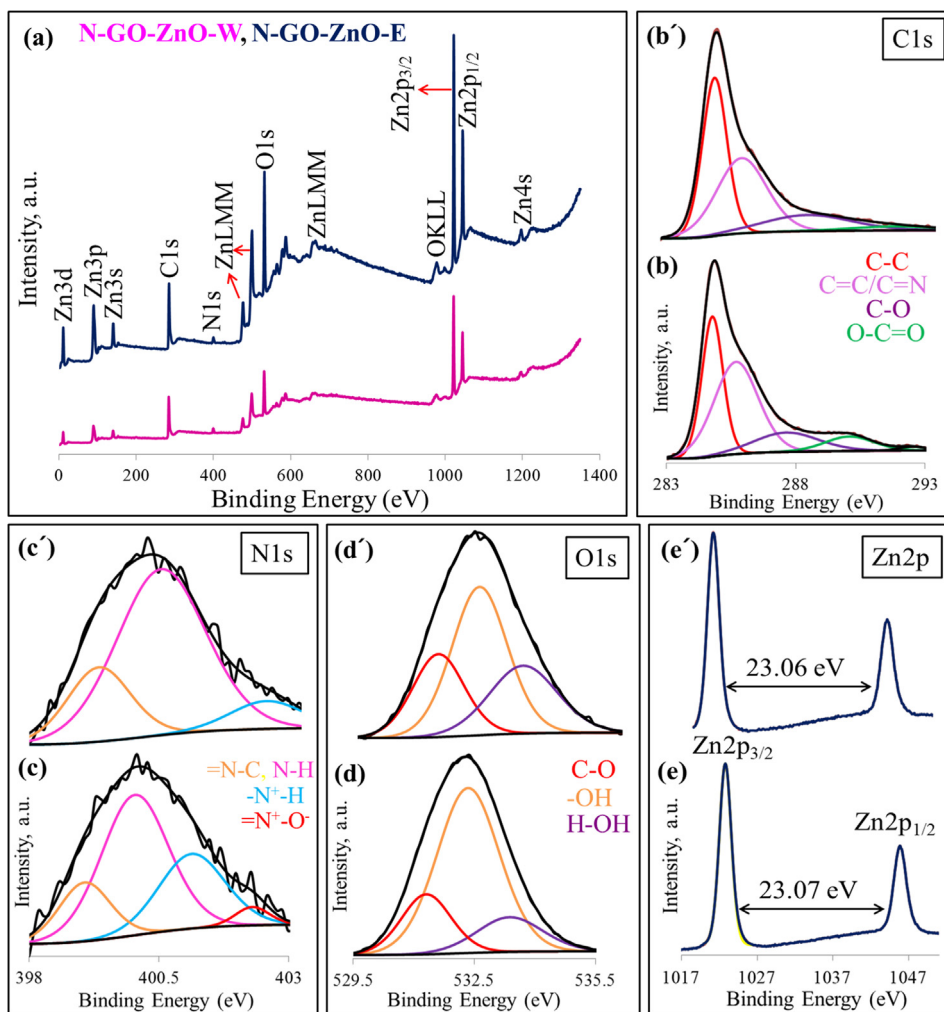


Fig. 3. (a) XPS spectrum of the *N*-GO-ZnO-W and *N*-GO-ZnO-E nanomaterial. Core-level spectra of, *N*-GO-ZnO-E (b) C1s, (c) N1s, (d) O1s, (e) Zn2p, and *N*-GO-ZnO-W (b') C1s, (c') N1s, (d') O1s, and (e') Zn2p.

pyrrolic-N intensities in Fig. 3c'. The deconvolution analysis of Zn2p in Fig. 3e (*N*-GO-ZnO-E) and e' (*N*-GO-ZnO-W) showed a doublet of low and high binding energy peaks corresponding to Zn2p_{3/2} and Zn2p_{1/2} respectively. The Zn2p_{3/2} (1022.78 eV) and Zn2p_{1/2} (1044.73 eV) peaks of *N*-GO-ZnO-E and Zn2p_{3/2} (1022.9 eV) and Zn2p_{1/2} (1044.86 eV) peaks of *N*-GO-ZnO-W were attributed to Zn²⁺ (≥ 1021.90 eV) oxidation state rather than metallic Zn–Zn bond (≤ 1021.45 eV) [32,35,40]. The difference in individual binding energies of both nanomaterials is due to the difference in charge transfer between Zn²⁺ to O²⁻, which are surrounded in a different chemical environment. Further, the spin-orbit splitting of 23.07 (Fig. 3e) and 23.06 eV (Fig. 3e') between Zn2p_{3/2} and Zn2p_{1/2} of *N*-GO-ZnO-E and *N*-GO-ZnO-W respectively stamped the presence of pure +2 oxidation state [40].

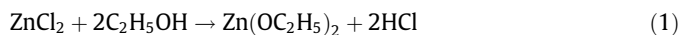
3.2. Mechanism of ZnO nanorods synthesis via HRTEM analysis

Fig. 4 shows the comparison of HRTEM images of *N*-GO-ZnO-E, *N*-GO-ZnO-W, and GO-ZnO-E at different magnifications. *N*-GO-ZnO-W showed around 20% of the ZnO nanorods population in comparison to the immense nanorods population of *N*-GO-ZnO-E. The magnified images of *N*-GO-ZnO-W (Fig. 4a'–e') showed shorter and broader nanorods, while *N*-GO-ZnO-E (Fig. 4a–e) revealed pointy and elongated nanorods. However, the NP size was almost similar in both nanomaterials (Fig. 4f, g (*N*-GO-ZnO-E) and f', g' (*N*-GO-ZnO-W)).

The only difference between two nanomaterials is the solvent, in which zinc precursor was dissolved and added. There are several important parameters in a solvent such as, dielectric constant, viscosity, surface tension, and pH, which play a crucial role in governing the production, dispersion, and morphology of a NP. The mechanism of ZnO nanorods formation in both nanomaterials (*N*-GO-ZnO-W and *N*-GO-ZnO-E) is divided into following four steps:

3.2.1. (I) monomer (ZnO) formation

In case of *N*-GO-ZnO-E, reaction between ZnCl₂ and C₂H₅OH resulted in the formation of Zn(ethoxide)₂ from the conjugate base of ethanol (–OC₂H₅). The alkoxide group made metal alkoxides very susceptible to hydrolysis, condensation, and nucleophilic reactions which usually follow alcoxolation and/or oxolation reaction to produce metal oxide [41]. The thermodynamics of these reactions depends on the strength of the entering nucleophile, the electrophilicity of metal, and on the partial charge and stability of the leaving group [42]. Herein, for coordinately saturated Zn (OC₂H₅)₂ in the absence of a catalyst, hydrolysis has occurred by the attack of a nucleophile, resulting in the formation of Zn(OH)₂, which followed either alcoxolation or oxolation to initiate the formation of ZnO monomer by the removal of a proton.



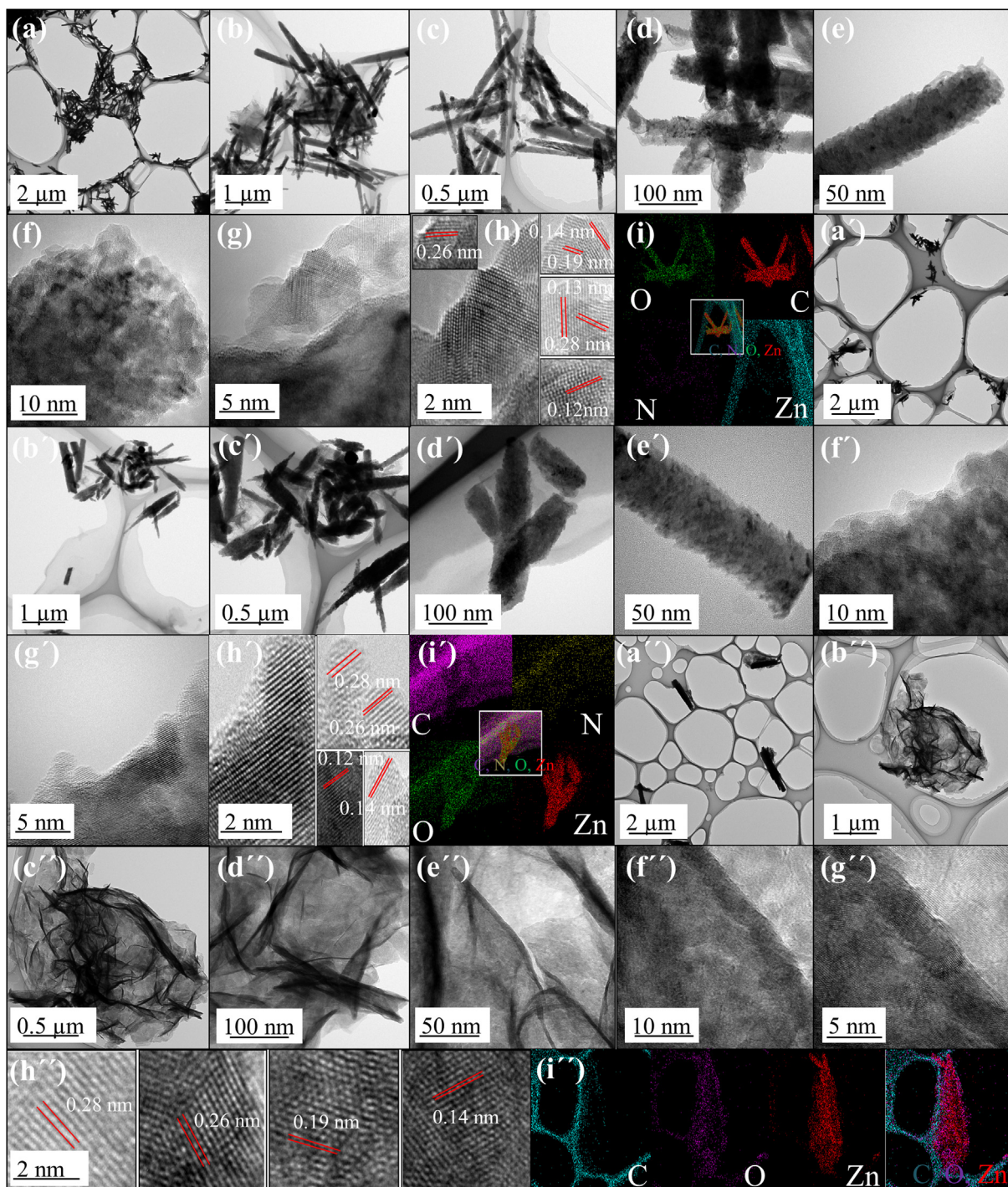
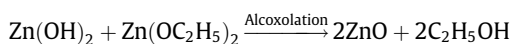
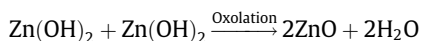
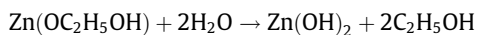
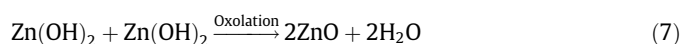
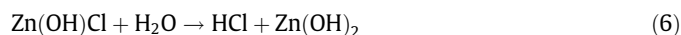


Fig. 4. HRTEM images of (a) *N*-GO-ZnO-E (b, c, and d) ZnO nanorods on *N*-GO surface at different magnifications, (e) magnified image of a single ZnO nanorod on *N*-GO, (f and g) magnified image of ZnO NPs in a single nanorod, (h) lattice line of the ZnO NPs in *N*-GO-ZnO-E, (i) EDX elemental mapping of C, N, O, and Zn. HRTEM images of (a') *N*-GO-ZnO-W (b', c', and d') ZnO nanorods on *N*-GO surface at different magnifications, (e') magnified image of a single ZnO nanorod on *N*-GO, (f' and g') magnified image of ZnO NPs in a single nanorod, (h') lattice line of the ZnO NPs in *N*-GO-ZnO-W, (i') EDX elemental mapping of C, N, O, and Zn. HRTEM images of (a'') GO-ZnO-E (b'', c'', and d'') ZnO nanorods on GO surface at different magnifications, (e'') magnified image of a single ZnO nanorod on GO, (f'' and g'') magnified image of ZnO NPs in a single nanorod and on GO surface, (h'') lattice line of the ZnO NPs in GO-ZnO-E, (i'') EDX elemental mapping of C, O, and Zn.



On the other hand, in case of *N*-GO-ZnO-W, an aqua complex of Zn (hydroxy)chloride was formed by the reaction of ZnCl_2 and H_2O . The aqua complex was later on hydrolyzed by reacting with second H_2O molecule resulting in the formation of $\text{Zn}(\text{OH})_2$. Finally, the $\text{Zn}(\text{OH})_2$ underwent either oxolation or simple condensation due to heating to produce ZnO [43].





3.2.2. (II) nucleation of ZnO

After the formation of initial ZnO monomer, the nucleation threshold started to build-up depending on the rate of supersaturation, which in turn is dependent on the solubility of the ZnO in the solvent. The solubility of any monomer in a chemical system is directly proportional to the dielectric constant of the solvent [44]. As we know, the dielectric constant of water ($\epsilon = 80$) is higher than ethanol ($\epsilon = 25$); therefore higher ZnO monomer solubility in N-GO-ZnO-W nanomaterial has led to its supersaturation reduction, and subsequent nucleation rate. Conversely, the decrease in surface energy due to a better ethanol-ZnO interaction, the relatively higher ZnO stability in N-GO-ZnO-E resulted in a massive supersaturation and increased nucleation rate. Herein, it is important to note that the monomer formation in both cases was strongly enhanced by the presence of different nitrogen configurations. This has altered the electronic environment of GO, enhanced the system reactivity which led to the generation of a higher number of monomer, accelerated nucleation rate, and finally produced smaller particles with narrower size distribution [30]. However, the eventual survival battle of a monomer is with the dielectric constant of its solvent which determines the final number of nuclei for growth. The mechanism of nucleation in both nanomaterials is shown in Fig. 5a.

3.2.3. (III) ZnO nanorods formation

After sufficient nucleation, ZnO nuclei undergo agglomeration to form particles. These ZnO NPs get crystallize into hexagonal discs either by NPs diffusion, by the surface reaction or by both mechanisms. The NPs self-assembly depends on the inter-particle

distance, particle interaction with solvent, and chemically or physically adsorbed organic/inorganic ions. We believe that the presence of different nitrogen configurations in both nanomaterials is crucial for a surface-integration controlled growth and stabilization of the nanocrystal. A 2 nm HRTEM images of N-GO-ZnO-E (Fig. 4h), and N-GO-ZnO-W (Fig. 4h') showed a lattice line of 0.12, 0.13, 0.14, 0.19, 0.25, 0.28 nm, depicting a Wurtzite-type structure of ZnO nanorods [45], which also confirmed the XRD findings (Fig. 2). Wurtzite crystal structure present hexagonal polar repeated units due to the difference in surface energy of its crystal faces [46]. The top plane of the crystal structure is positively terminated Zn^{2+} (0 0 0 1) while the bottom is surrounded by negatively terminated O^{2-} (0 0 0 $\bar{1}$) atoms. These repeated polar units are perpendicular to c-axis (0 0 0 2), which is a layer of side atoms to enclose the crystal. The sequential layering of Zn^{2+} and O^{2-} atoms along the c axis gives rise to intrinsic polarity. The difference in surface energy between (0 0 0 1) and side surfaces favours anisotropic crystal growth along c-axis, thus; resulting in a rod-like morphology. The inherited instability of the (0 0 0 1) and (0 0 0 $\bar{1}$) faces requires additional respective complementary charges to stabilize the system [47]. The difference in chemisorption of different molecules, atoms onto ZnO, directs NP morphology differently which subsequently defines chemical properties of the nanomaterial. Similarly, herein, the interaction of different nitrogen configurations (pyrrolic, pyridinic, graphitic-N, and pyridinic- N^+O^-) and solvent (ethanol and water) with ZnO will determine the Debye length, surface potential barrier height, surface charge and its layer thickness.

- (i) Following types of interactions are possible between pyrrolic, pyridinic, graphitic-N, pyridinic- N^+O^- , ZnO, and ethanol/water (Fig. 5b). The XPS analysis of N-GO-ZnO-W (Fig. 3c') and N-GO-ZnO-E (Fig. 3c) has revealed the presence of pyridinic, pyrrolic, graphitic-N along with an additional pyridinic- N^+O^- peak in latter. The lone pair of Pyridinic-N has interacted with O of ZnO, which resulted in the generation

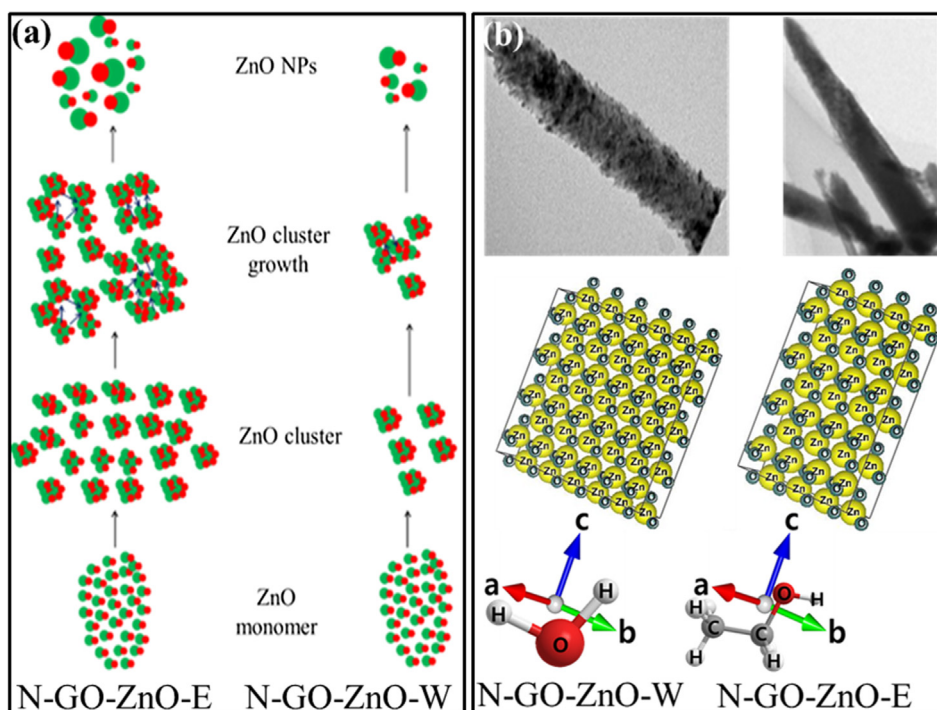


Fig. 5. (a) Nucleation and formation of initial ZnO NPs, (b) ZnO NPs stacking orientation governed by water and ethanol molecular geometry in N-GO-ZnO-W and N-GO-ZnO-E. Three dimensional (a, b, and c-axis) directions in this figure were in accordance with the wurtzite crystal system of ZnO shown in the figure b.

of pyridinic- N^+O^- in *N*-GO-ZnO-E, but in case of *N*-GO-ZnO-W, the higher polarity of water has increased the shielding effect of pyridinic-N [48]; thus, justifying the absence of pyridinic- N^+O^- peak in its XPS spectra.

- (ii) Pyrrolic-N is a H bond donor due to the availability of acidic-H. The electronegative O atoms of ZnO, and $C_2H_5-O-H/H-O-H$ are H-bond acceptor for the acidic-H of Pyrrolic-N.
- (iii) Graphitic-N is a H bond acceptor due to the absence of acidic-H and will accept a H from Pyrrolic-N, and $H-O-H/H-O-C_2H_5$.
- (iv) Pyridinic-N has a lone pair so it will be a H-bond acceptor for the $H-OC_2H_5$ and pyrrolic-N.
- (v) The O^- of pyridinic- N^+O^- will accept a H-bond from $H-OC_2H_5$ and pyrrolic-N.
- (vi) The inter-molecular H-bonding between $H-O-H$ and $H-OC_2H_5$ is likely to occur in *N*-GO-ZnO-W and *N*-GO-ZnO-E respectively.

As Zn and O atoms of ZnO are forming consecutive layered structures [48], therefore these interactions among a growing crystal surface will act as a substrate for the next layer of ZnO. The extent of interactions along c-axis will determine the length of the ZnO nanorods, while the interactions along m-plane will define the width of ZnO nanorods which we believe are dependent on the geometry of

the solvent molecules (ethanol, water). If we have a look at the structure of water and ethanol, H_2O has a bent structure and 3 atoms to propagate the surface interactions in three directions. Both H and O atom of H_2O will propagate interactions with ZnO either along c-axis or m-plane. Contrarily, in ethanol, there are only two interacting atoms; a single O and a single H which will further the interactions either along c-axis or m-plane. m-plane interactions on another side of $H-OC_2H_5$ are stopped due to the attachment of C_2H_5 at the end of the molecule. C_2H_5 is acting as a dead-end to advance the interactions along m-plane which resulted in the formation of ZnO nanorods with a high aspect ratio (high length and short width) in *N*-GO-ZnO-E. H_2O has more atoms to propagate interaction in m-plane than $H-OC_2H_5$, therefore, ZnO nanorods with a low aspect ratio (short height and high width) were obtained in *N*-GO-ZnO-W. Besides the absence of pyridinic-N interactions with ZnO and $H-O-H$ (absence of pyridinic- N^+O^- shown by XPS) has also significantly reduced the ZnO stacking along c-axis.

3.2.4. (IV) final dispersion of ZnO nanorods

ZnO nanorods in both nanomaterials showed severe aggregation due to high surface energy of individual nanorods. The growth mechanism of ZnO nanorods in *N*-GO-ZnO-W and *N*-GO-ZnO-E is presented in Fig. 5b. To confirm the influence of nitrogen doping in the production and stabilization of initial ZnO monomers, ZnO

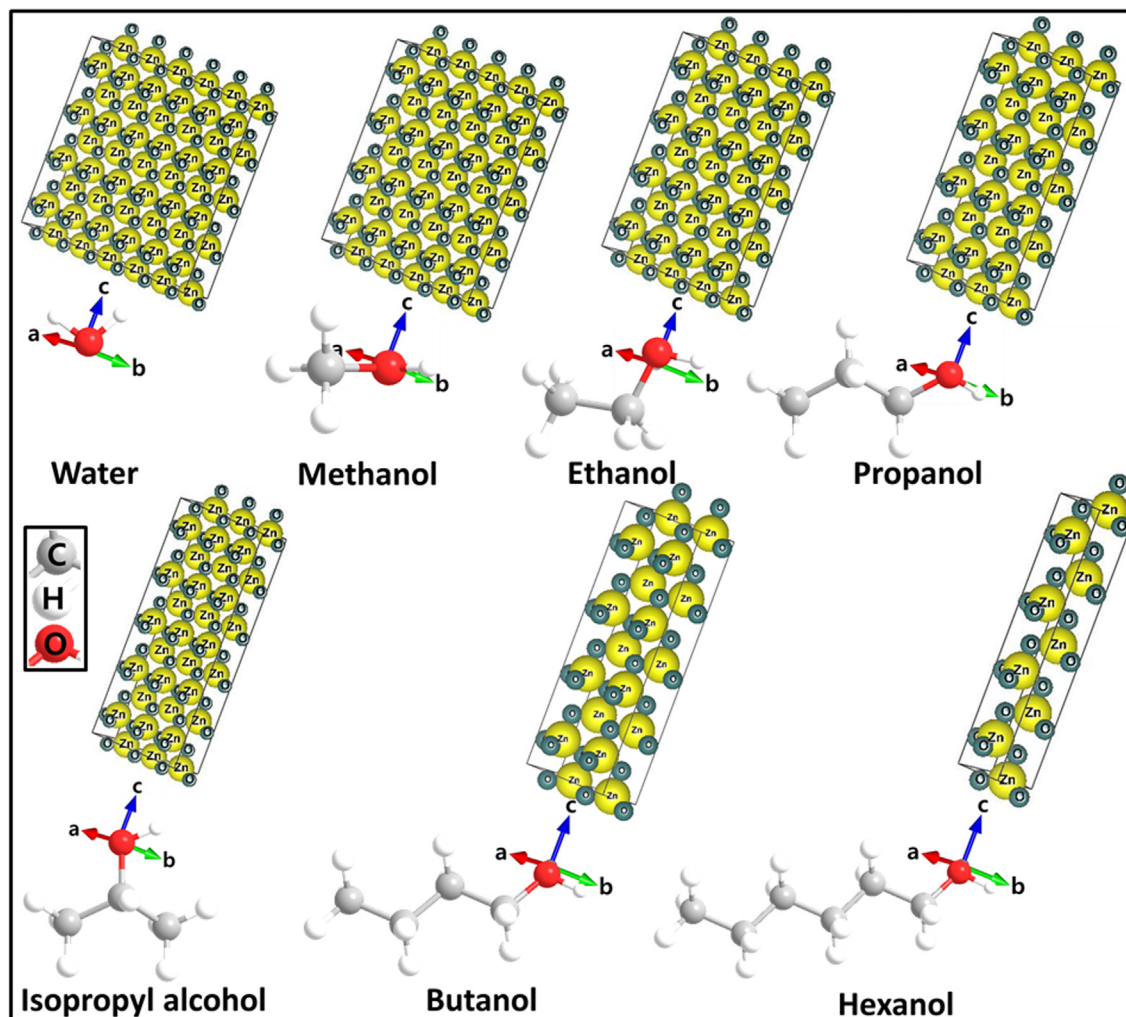


Fig. 6. ZnO NPs stacking orientation in wurtzite crystal system of ZnO nanorods governed by different solvent molecular geometry. Three dimensional (a, b, and c-axis) directions in this figure were in accordance with the wurtzite crystal system of ZnO shown in this figure.

nanorods were synthesized exclusively on the GO surface (Fig. 4a''). Fig. 4(b''–d''), shows a decent population of intermingled ZnO NPs in the form of sharp, pointy, and slightly bent nanorods onto GO sheets. The width of the nanorods was very less in comparison to *N*-GO-ZnO-E and *N*-GO-ZnO-W nanomaterials. This suggests that after initial adsorption of ZnO NPs on electrophilic centers of GO, ethanol solvent facilitated ZnO NPs stacking along *c*-axis. The adsorption of ZnO NPs on neighboring substrate surfaces was low due to the absence of ample electrophilic centers. Thus; the width of the nanorods was not only hampered by the structural configuration of ethanol but also due to the absence of nitrogen configurations (Fig. 4c''–e''). Further, the lattice line of *N*-GO-ZnO-W (Fig. 4h'), *N*-GO-ZnO-E (Fig. 4h), GO-ZnO-E (Fig. 4h'') showed a very interesting behavior by assembling ZnO NPs in an oriented (OA) and non-oriented attachment (NOA) fashion for the latter two nanomaterials respectively, which differs in terms of the orientation of their crystal lattice at the grain boundary [8]. *N*-GO-ZnO-E and GO-ZnO-E showed no specific preference in attachment, while in *N*-GO-ZnO-W, a particular crystallographic alignment has occurred by rotation until the perfect crystal phase of two NPs or a twin matched in a minimum energy configuration to allow for continuous crystallographic planes. The high dielectric constant of H₂O has induced strong attractive forces in interatomic interactions of the attaching NPs and other attaching surfaces. This attractive force is the actual driving forces to overcome the energy barrier for oriented particle-particle contact [8]. The successful synthesis of *N*-GO-ZnO-E, *N*-GO-ZnO-W, and GO-ZnO-E was ensured from elemental mapping as shown in Fig. 4i, i' and i'' respectively.

This detailed spectroscopic analysis shows that ZnO nanorods obtained in the presence of ethanol showed a higher aspect ratio, while it was lower in the presence of water. Besides, the population of ZnO nanorods in both cases was attributed to the dielectric constant of water and ethanol as explained above in detail and shown in Fig. 5a. The obtained results conclude that the number of functional atoms in water are present in three dimensions (*a*, *b* and *c*-axis) and therefore they can coordinate with the metal ions in all possible directions of wurtzite hexagonal crystal system of ZnO, leading to lower aspect ratio nanorods. However, in the case of ethanol, the unavailability of binding sites along *a*-axis provides a size-limiting effect for the ZnO NPs stacking along *a*-axis, thus leading to preferred growth along *b* and *c*-axis and eventually generating ZnO nanorods with a higher aspect ratio as shown in Fig. 5b. By following this theory, Fig. 6 has been made from the ZnO nanorods reported in the literature with methanol, ethanol, propanol, isopropanol, butanol, hexanol, and water to evaluate the applicability of presented theory with other solvent systems [49–61]. This analysis suggests the successful validation of the proposed theory. For example, the ZnO nanorods reported by Samulski et al. with methanol have a higher aspect ratio in comparison to the one obtained in our study using water [51]. The unavailability of binding site along *a*-axis in methanol result into nanorods with reduced width. In the case of water, the availability of binding site along 3-dimensions result in ZnO nanorods with a comparatively lower aspect ratio. Similar pattern can be noted from other reports as well. For example, the aspect ratio of ZnO nanorods linearly increase with the increase in carbon chain from methanol to hexanol. The reason behind this behavior is the steric hindrance caused by long-chain carbon atoms which are inactive and prevent further stacking of ZnO NPs in the direction of the carbon chain, thus escalating ZnO nanorod growth only along *b* and *c*-axis (as shown in Fig. 6) and eventually leading to a high aspect ratio ZnO nanorods. Even, nanorods obtained with hexanol showed a needle-like structure [58]. These observations reflect that the optimum conditions to obtain the desired aspect ratio of nanorods is not only a perfect selection of solvent molecular geometry but also

the length of the carbon chain and steric hindrance is of equal and utmost importance.

4. Conclusion

The study concludes an interesting new finding regarding the influence of solvent (water and ethanol) molecular geometry on the controlled growth of ZnO nanorods. Herein we provided a detailed discussion about a series of individual factors such as surface tension, dielectric constant, pH, and viscosity of a solvent that are involved right from the synthesis of initial monomer to the final growth into a particular morphology. Further, the paper describes how the geometry of water and ethanol determines the aspect ratio of the ZnO nanorods and how replacing ethanol with water (ZnO precursor dissolving solvent) resulted in a steep decrease in ZnO nanorods population by ~80%. The possible synthesis and dispersion route of ZnO nanorods was explored on a GO and a nitrogen-doped GO surface to understand the involvement of nitrogen in the production of the ZnO monomer. We unveiled a new way to predict and design the morphology of nanostructures by selecting a solvent of a particular molecular geometry. The study also reveals that the optimum conditions to obtain the desired aspect ratio of nanorods is not only about a perfect selection of solvent molecular geometry but also the length of the carbon chain and steric hindrance is of equal and utmost importance. The proposed growth theory was also validated with previously reported ZnO nanorods systems and showed a satisfactory validation which presents a substantial improvement in terms of predicting and designing different NP morphologies simply by selecting a solvent with a specific molecular geometry. In this regard, the present study could be further extended in the future for other metal oxide nanorods and other morphologies such as nanocubes, nanospindle, nanocones, nanocombs, and nanoflowers.

CRediT authorship contribution statement

Ammara Ejaz: Conceptualization, Methodology, Validation, Formal analysis, Investigation, Writing - original draft, Writing - Review & Editing. **Jong H. Han:** Resources, Data curation, Writing - original draft, Writing - Review & Editing, Formal analysis, Visualization, Supervision, Project administration. **Ravinder Dahiya:** Formal analysis, Writing - review & editing, Visualization.

Declaration of Competing Interest

There are no conflicts to declare.

Acknowledgements

^aThis work was supported in part by Engineering and Physical Sciences Research Council (EPSRC) through Engineering Fellowship for Growth (EP/R029644/1 and EP/M002527/1), and North West Centre for Advanced Manufacturing (NW CAM) project supported by the European Union's INTERREG VA Programme (H2020-Interreg-IVA5055), managed by the Special EU Programmes Body (SEUPB). The views and opinions in this document do not necessarily reflect those of the European Commission or the SEUPB. ^bThis work was supported in part by Priority Research Centers Program through the National Research Foundation of Korea (NRF) funded by the Ministry of Education, Science, and Technology (2018R1A6A1A03024334), Nano Material Technology Development Program through the NRF funded by the Ministry of Science, ICT, and Future Planning (2017M3A7B4014045) and by Trade, Industry & Energy (MOTIE, Korea) under Industrial Technology Innovation Program (No. 10052838).

Appendix A. Supplementary material

Supplementary data to this article can be found online at <https://doi.org/10.1016/j.jcis.2020.02.117>.

References

- [1] L. Vayssieres, Growth of arrayed nanorods and nanowires of ZnO from aqueous solutions, *Adv. Mater.* 15 (5) (2003) 464–466.
- [2] K. Ocakoglu, S.A. Mansour, S. Yildirimcan, A.A. Al-Ghamdi, F. El-Tantawy, F. Yakuphanoglu, Microwave-assisted hydrothermal synthesis and characterization of ZnO nanorods, *Spectrochim. Acta A* 148 (2015) 362–368.
- [3] J. Li, H. Liu, H. Fu, L. Xu, H. Jin, X. Zhang, L. Wang, K. Yu, Synthesis of 1D α -MoO₃/0D ZnO heterostructure nanobelts with enhanced gas sensing properties, *J. Alloys Compd.* 788 (2019) 248–256.
- [4] Yong Ding, Jia Xu, Lei Chen, Jianxi Yao, Songyuan Dai, Jihuai Wu, Tasawar Hayat, Ahmed Alsaedi, Pierced ZnO nanosheets via a template-free photopolymerization in microemulsion, *J. Alloys Compd.* 787 (2019) 779–785, <https://doi.org/10.1016/j.jallcom.2019.02.107>.
- [5] Y.-C. Chang, Complex ZnO/ZnS nanocable and nanotube arrays with high performance photocatalytic activity, *J. Alloys Compd.* 664 (2019) 538–546.
- [6] Q. Zhang, W. Bai, Synthesis and growth mechanism of macroscopic ZnO nanocombs and nanobelts, *Vacuum* 86 (4) (2011) 398–402.
- [7] C. Ray, T. Pal, Recent advances of metal–metal oxide nanocomposites and their tailored nanostructures in numerous catalytic applications, *J. Mater. Chem. A* 5 (20) (2017) 9465–9487.
- [8] K.M. Ezealisiji, X. Siwe-Noundou, B. Maduelosi, N. Nwachukwu, R.W.M. Krause, Green synthesis of zinc oxide nanoparticles using *Solanum torvum* (L) leaf extract and evaluation of the toxicological profile of the ZnO nanoparticles–hydrogel composite in Wistar albino rats, *Int. Nano Lett.* 9 (2) (2019) 99–107.
- [9] L. Manjakkal, B. Sakthivel, N. Gopalakrishnan, R. Dahiya, Printed flexible electrochemical pH sensors based on CuO nanorods, *Sens. Actuator B-Chem.* 2018 (263) (2018) 50–58.
- [10] L. Manjakkal, C.G. Núñez, W. Dang, R. Dahiya, Flexible self-charging supercapacitor based on graphene-Ag-3D graphene foam electrodes, *Nano Energy* 51 (2018) 604–612.
- [11] W. Dang, L. Manjakkal, W.T. Navaraj, L. Lorenzelli, V. Vinciguerra, R. Dahiya, Stretchable wireless system for sweat pH monitoring, *Biosens. Bioelectron.* 107 (2018) 192–202.
- [12] L. Manjakkal, D. Shakhivel, R. Dahiya, Flexible printed reference electrodes for electrochemical applications, *Adv. Mater. Technol.* 3 (12) (2018) 1800252.
- [13] D.P. Singh, Synthesis and growth of ZnO nanowires, *Sci. Adv. Mater.* 2 (3) (2010) 245–272.
- [14] P.K. Bavisar, P.R. Nikam, S.S. Gargote, A. Ennaoui, B.R. Sankapal, Controlled synthesis of ZnO nanostructures with assorted morphologies via simple solution chemistry, *J. Alloys Compd.* 551 (2013) 233–242.
- [15] M. Sui, P. Gong, X. Gu, Review on one-dimensional ZnO nanostructures for electron field emitters, *Front. Optoelectron.* 6 (4) (2013) 386–412.
- [16] S. Baruah, J. Dutta, Hydrothermal growth of ZnO nanostructures, *Sci. Technol. Adv. Mater.* 10 (1) (2009) 013001. 1–18.
- [17] T. Pauporté, Design of solution-grown ZnO nanostructures, in: Z.M. Wang (Ed.), *Toward functional nanomaterials*, Springer US, New York, NY, 2009, p. 77.
- [18] S. Xu, Z.L. Wang, One-dimensional ZnO nanostructures: solution growth and functional properties, *Nano Res.* 4 (11) (2011) 1013–1098.
- [19] M. Niederberger, H. Cölfen, Oriented attachment and mesocrystals: non-classical crystallization mechanisms based on nanoparticle assembly, *Phys. Chem. Chem. Phys.* 8 (28) (2006) 3271–3287.
- [20] Z.L. Wang, ZnO nanowire and nanobelt platform for nanotechnology, *Mater. Sci. Eng. R Rep.* 64 (3) (2009) 33–71.
- [21] A.B. Djurišić, X. Chen, Y.H. Leung, A. Man Ching Ng, ZnO nanostructures: growth, properties and applications, *J. Mater. Chem. A* 22 (14) (2012) 6526–6535.
- [22] S.K. Arya, S. Saha, J.E. Ramirez-Vick, V. Gupta, S. Bhansali, S.P. Singh, Recent advances in ZnO nanostructures and thin films for biosensor applications: review, *Anal. Chim. Acta* 737 (2012) 1–21.
- [23] L. Loh, S. Dunn, Recent progress in ZnO-based nanostructured ceramics in solar cell applications, *J. Nanosci. Nanotechnol.* 12 (11) (2012) 8215–8230.
- [24] S. Sun, X. Zhang, J. Zhang, X. Song, Z. Yang, Unusual designated-tailoring on zone-axis preferential growth of surfactant-free ZnO mesocrystals, *Cryst. Growth Des.* 12 (5) (2012) 2411–2418.
- [25] Y. Zhang, X. Yan, Y. Yang, Y. Huang, Q. Liao, J. Qi, Scanning probe study on the piezotronic effect in ZnO nanomaterials and nanodevices, *Adv. Mater.* 4 (34) (2012) 4647–4655.
- [26] A. Ejaz, S. Jeon, The insight study of SnO pico size particles in an ethanol-water system followed by its biosensing application, *Biosens. Bioelectron.* 117 (2018) 129–137.
- [27] A. Ejaz, S. Jeon, The individual role of pyrrolic, pyridinic and graphitic nitrogen in the growth kinetics of Pd NPs on N-rGO followed by a comprehensive study on ORR, *Int. J. Hydrog. Energy* 43 (11) (2018) 5690–5702.
- [28] A. Ejaz, S. Jeon, Electrooxidation of N₂H₄ through CuCuO electronic oscillation on a nitrogen-doped GO surface, *Sens. Actuat. B, Chem.* 284 (2019) 494–504.
- [29] M.A. Kafi, A. Paul, A. Vilouras, R. Dahiya, Mesoporous chitosan based conformable and resorbable biostrip for dopamine detection, *Biosens. Bioelectron.* 147 (2020) 111781.
- [30] M.A. Kafi, K. Aktar, M. Todo, R. Dahiya, Engineered chitosan for improved 3D tissue growth through Paxillin-FAK-ERK activation, *Regen. Biomater.* (2019) 1–11.
- [31] A. Ejaz, Y. Joo, J.C. Cho, J.M. Choi, J.Y. Kim, S. Lee, S. Jeon, Synthesis and catalytic activity of Ag nanoparticles dispersed on nitrogen-doped GOPx toward direct electrooxidation of formaldehyde, *J. Electroanal. Chem.* 813 (2018) 31–38.
- [32] C.D. Wanger, W.M. Riggs, L.E. Davis, J.F. Moulder, Muilenberg Perkin-Elmer Corp G. E. Handbook of X-ray Photoelectron Spectroscopy, Physical Electronics Division, Eden Prairie, Minnesota, USA, 1979. 190 pp. Briggs, *Surf. Interface Anal.* 3 (4) (1981) 5.
- [33] A. Ejaz, S. Jeon, A highly stable and sensitive GO-XDA-Mn₂O₃ electrochemical sensor for simultaneous electrooxidation of paracetamol and ascorbic acid, *Electrochim. Acta* 245 (2017) 742–751.
- [34] A. Ejaz, Y. Joo, S. Jeon, Fabrication of 1,4-bis(aminomethyl)benzene and cobalt hydroxide @ graphene oxide for selective detection of dopamine in the presence of ascorbic acid and serotonin, *Sens. Actuat. B, Chem.* 240 (2017) 297–307.
- [35] X. Wang, J. Hao, Y. Su, F. Liu, J. An, J. Lian, A Ni_{1-x}Zn_xS/Ni foam composite electrode with multi-layers: one-step synthesis and high supercapacitor performance, *J. Mater. Chem. A* 4 (33) (2016) 12929–12939.
- [36] H. Wang, T. Maiyalagan, X. Wang, Review on recent progress in nitrogen-doped graphene: synthesis, characterization, and its potential applications, *ACS Catal.* 2 (5) (2012) 781–794.
- [37] S. Cobo, J. Heidkamp, P.A. Jacques, J. Fize, V. Fourmond, L. Guetaz, B. Jousseme, V. Ivanova, H. Dau, S. Palacin, M. Fontecave, V. Artero, A Janus cobalt-based catalytic material for electro-splitting of water, *Nat. Mater.* 11 (9) (2012) 802–807.
- [38] A. Ejaz, M.S. Ahmed, S. Jeon, Synergistic effect of 1,4-benzenedimethanamine assembled graphene supported palladium for formaldehyde oxidation reaction in alkaline media, *J. Electrochem. Soc.* 163 (5) (2016) B163–B168.
- [39] J. Yu, L. Zhu, C. Fan, C. Zan, L. Hu, S. Yang, Q. Zhang, W. Zhu, L. Shi, F. Wei, Highly dispersed Mn₂O₃ microspheres: Facile solvothermal synthesis and their application as Li-ion battery anodes, *Particuology* 22 (2015) 89–94.
- [40] S. Rajendran, M.M. Khan, F. Gracia, J. Qin, V.K. Gupta, S. Arumainathan, Ce³⁺-ion induced visible-light photocatalytic degradation and electrochemical activity of ZnO/CeO₂ nanocomposite, *Sci. Rep.* 6 (31641) (2016) 1–11.
- [41] M. Matsuo, Japanese patent, 88100032, A2; JP 63100032, May 2, 1988.
- [42] T. Takeuchi, Japanese Patent 88117919 A2; JP 63117919, 1988.
- [43] A. Moezzi, M. Cortie, A. McDonagh, Transformation of zinc hydroxide chloride monohydrate to crystalline zinc oxide, *Dalton Trans.* 45 (17) (2016) 7385–7390.
- [44] G. Oskam, Fd.J.P.J. Poot, Synthesis of ZnO and TiO₂ nanoparticles, *Sol-Gel, Sci. Technol.* 37 (3) (2006) 157–160.
- [45] S.B. Rana, V.K. Bhardwaj, S. Singh, A. Singh, N. Kaur, Influence of surface modification by 2-aminothiophenol on optoelectronic properties of ZnO nanoparticles, *J. Exp. Nanosci.* 9 (9) (2014) 877–891.
- [46] C. Jagadish, S.J. Pearton, Zinc Oxide Bulk, Thin Films and Nanostructures: Processing, Properties, and Applications, Elsevier, 2011.
- [47] A. Moezzi, A.M. McDonagh, M.B. Cortie, Zinc oxide particles: synthesis, properties and applications, *Chem. Eng.* 185–186 (2012) 1–22.
- [48] M. Witanowski, Z. Biedrzycka, W. Sicinska, Z. Grabowski, A study of solvent polarity and hydrogen bonding effects on the nitrogen NMR shielding of isomeric tetrazoles and initial calculation of the nitrogen shielding of azole systems, *J. Magn. Reson.* 131 (1) (1998) 54–60.
- [49] P.B. Khoza, M.J. Moloto, L.M. Sikhivihlu, The effect of solvents, acetone, water, and ethanol, on the morphological and optical properties of ZnO nanoparticles prepared by microwave, *J. Nanotechnol.* 2012 (2012) 1–6.
- [50] A. Ali, S. Ambreen, R. Javed, S. Tabassum Ul Haq, M. Zia, ZnO nanostructure fabrication in different solvents transforms physico-chemical, biological and photodegradable properties, *Mater. Sci. Eng. C Mater. Biol. Appl.* 74 (2017) 137–145.
- [51] B. Cheng, E.T. Samulski, Hydrothermal synthesis of one-dimensional ZnO nanostructures with different aspect ratios, *ChemComm.* 8 (2004) 986–987.
- [52] H.L. Cao, X.F. Qian, Q. Gong, W.M. Du, X.D. Ma, Z.K. Zhu, Shape- and size-controlled synthesis of nanometre ZnO from a simple solution route at room temperature, *Nanotechnology* 17 (15) (2006) 3632–3636.
- [53] R. Idiwati, N. Mufti, A. Taufiq, H. Wisodo, I.K.R. Laila, A. Sunaryono-Fuad, Effect of growth time on the characteristics of ZnO nanorods, *IOP Conf. Ser. Mater. Sci. Eng.* 202 (012050) (2017) 1–8.
- [54] M. Hadiyan, A. Salehi, A. Koohi-Saadi, Sub-ppm acetone gas sensing properties of free-standing ZnO nanorods, *J. Electroceramics* 42 (3) (2019) 147–155.
- [55] Z.N. Urgessa, O.S. Oluwafemi, E.J. Olivier, J.H. Neethling, J.R. Botha, Synthesis of well-aligned ZnO nanorods on silicon substrate at lower temperature, *J. Alloys Compd.* 580 (2013) 120–124.
- [56] C. Pacholski, A. Kornowski, H. Weller, Self-assembly of ZnO: from nanodots to nanorods, *Proc. SPIE Int. Soc. Opt. Eng.* 5513 (2004) 232–241.
- [57] S. Wilken, D. Scheunemann, V. Wilkens, J. Parisi, H. Borchert, Improvement of ITO-free inverted polymer-based solar cells by using colloidal zinc oxide nanocrystals as electron-selective buffer layer, *Org. Electron.* 13 (11) (2012) 2386–2394.

- [58] Q.R. Hu, S.L. Wang, P. Jiang, H. Xu, Y. Zhang, W.H. Tang, Synthesis of ZnO nanostructures in organic solvents and their photoluminescence properties, *J. Alloys Compd.* 496 (1) (2010) 494–499.
- [59] J.L. Campbell, M. Breedon, K. Latham, K. Kalantar-zadeh, Electrowetting of superhydrophobic ZnO nanorods, *Langmuir* 24 (9) (2008) 5091–5098.
- [60] M. Breedon, M.B. Rahmani, S.H. Keshmiri, W. Wlodarski, K. Kalantar-zadeh, Aqueous synthesis of interconnected ZnO nanowires using spray pyrolysis deposited seed layers, *Mater. Lett.* 64 (2010) 291–294.
- [61] J. Tiwari, R.N. Tiwari, K.S. Kim, Zero-dimensional, one-dimensional, two-dimensional and three-dimensional nanostructured materials for advanced electrochemical energy devices, *Prog. Mater. Sci.* 57 (2012) 724–803.